

Effective and Robust Multimodal Medical Image Analysis

Joy Dhar

Indian Institute of Technology Ropar

Rupnagar, Punjab, India

joy.22csz0003@iitpr.ac.in

Nayyar Zaidi

Deakin University

Melbourne, Victoria, Australia

nayyar.zaidi@deakin.edu.au

Maryam Haghigheh

Queensland University of Technology

Brisbane, QLD, Australia

maryam.haghigheh@qut.edu.au

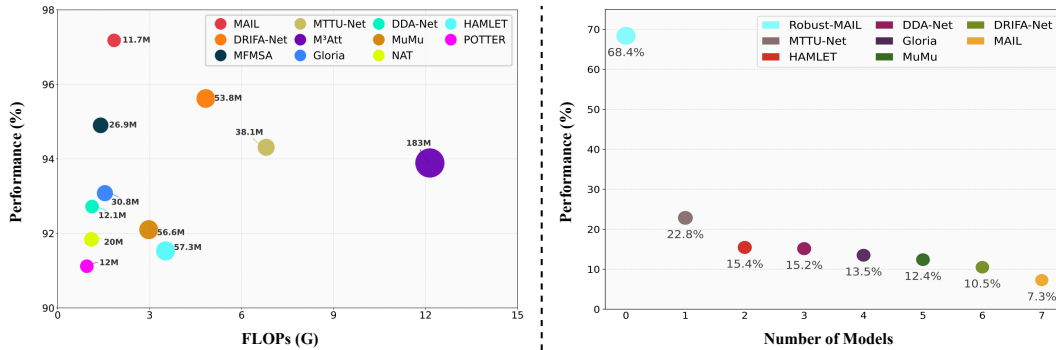


Figure 1: (Left) Cost–performance trade-off: comparison of our proposed MAIL framework vs. computationally-intensive fusion models (e.g., DRIFA-Net [12], MuMu [25]). (Right) Adversarial robustness: comparison of proposed Robust-MAIL vs. SOTA methods under a PGD attack.

Abstract

Multimodal Fusion Learning (MFL), leveraging disparate data from various imaging modalities (e.g., MRI, CT, SPECT), has shown great potential for addressing medical problems such as skin cancer and brain tumor prediction. However, existing MFL methods face three key limitations: a) they often specialize in specific modalities, and overlook effective shared complementary information across diverse modalities, hence limiting their generalizability for multi-disease analysis; b) they rely on computationally expensive models, restricting their applicability in resource-limited settings; and c) they lack robustness against adversarial attacks, compromising reliability in medical AI applications. To address these limitations, we propose a novel Multi-Attention Integration Learning (MAIL) network, incorporating two key components: a) an efficient residual learning attention block for capturing refined modality-specific multi-scale patterns and b) an efficient multimodal cross-attention module for learning enriched complementary shared representations across diverse modalities. Furthermore, to ensure adversarial robustness, we extend MAIL network to design Robust-MAIL by incorporating random projection filters and modulated attention noise. Extensive evaluations on 20 public datasets show that both MAIL and Robust-MAIL outperform existing methods, achieving performance gains of up to 9.34% while reducing computational costs by up to 78.3%. These results highlight the superiority of our approaches, ensuring more reliable predictions than top competitors. **Code:** <https://github.com/misti1203/MAIL-Robust-MAIL>.

Keywords

Medical Imaging, Adversarial Defenses, Multimodal Attention

ACM Reference Format:

Joy Dhar, Nayyar Zaidi, and Maryam Haghigheh. 2026. Effective and Robust Multimodal Medical Image Analysis. In *Proceedings of the 32nd ACM SIGKDD Conference on Knowledge Discovery and Data Mining V.1 (KDD '26), August 09–13, 2026, Jeju Island, Republic of Korea*. ACM, New York, NY, USA, 12 pages. <https://doi.org/10.1145/3770854.3780331>

1 Introduction

Many real-world applications rely fundamentally on multimodal data. A prime example is medical diagnostics where various modalities, such as magnetic resonance imaging (MRI), computed tomography scan (CT-scan), and chest x-ray (CXR), etc. play a crucial role in diagnosing critical health conditions, including brain tumors, various cancers, and other diseases. Recent advancements in deep learning for medical image analysis have revolutionized healthcare, offering rapid and cost-effective diagnostic solutions that improve decision-making for clinicians [17]. Existing methods [10, 11, 19, 44, 60] for handling multiple modalities, typically build models on a single modality and then apply strategies such as feature fusion and attention mechanisms to improve model performance. However, these approaches often result in suboptimal performance due to their lack of ability to effectively capture the most informative shared representations – primarily because of noise present in medical data and issues with overfitting.

How to devise an effective model that is capable of leveraging various modalities – also known as Multimodal Fusion Learning (MFL), remains an open challenge in the machine learning community. MFL learns information from multiple modalities to capture enhanced shared representations, thereby improving predictive performance [12, 24, 25]. These methods address key limitations



This work is licensed under a Creative Commons Attribution 4.0 International License.
KDD '26, Jeju Island, Republic of Korea
 © 2026 Copyright held by the owner/author(s).
 ACM ISBN 979-8-4007-2258-5/2026/08
<https://doi.org/10.1145/3770854.3780331>

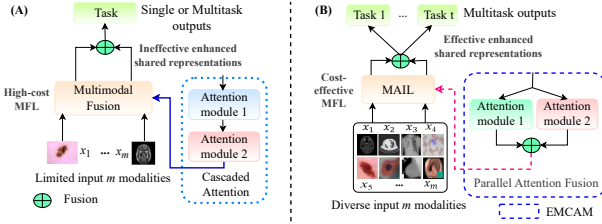


Figure 2: (A–B) Attention-alignment paradigms for MFL: cascaded attention (e.g., DRIFA-Net [12], MuMu [25]) vs. our parallel fusion attention (EMCAM in MAIL). The parallel design reduces information loss during shared-representation learning unlike cascaded pipelines.

faced by the above-mentioned single-modal learning models by capturing shared complementary representations from diverse modalities. However, these methods still face performance limitations due to their restricted ability to capture enriched representations, mainly because they do not incorporate attention mechanisms. In recent years, attention-based models have gained popularity for their ability to automatically learn the importance of individual tokens (i.e., elements of interest) [55]. Their application to MFL has shown promise, with several notable attention-based MFL approaches [7, 23, 24] being developed to enrich representations and improve performance across medical imaging modalities.

Despite the success of MFL methods, existing approaches usually face four fundamental challenges. First, compared to single-modal learning networks, existing MFL incurs **significantly higher computational costs** (*challenge 1*) due to computationally intensive convolutions or attention modules, posing substantial efficiency barriers that must be overcome for practical applications. Second, existing MFLs often process attention modules in a cascaded manner (e.g., sequentially stacking modules), which potentially **risks progressive information loss during transitions between modules** (*challenge 2*). This design choice can significantly degrade the retention of important representations. Third, current MFL approaches have **limited capacity to effectively learn shared complementary representations** (*challenge 3*) across diverse medical imaging modalities, regardless of whether they employ single attention mechanisms or cascaded multi-attention modules. This is because, their reliance on disease-specific modalities – such as MRI, PET, CT, SPECT, dermoscopy, or Pap smears (targeting brain disorders, skin/lung/cervical cancers) – during representation learning process, potentially **limits their generalizability** for multi-disease classification. Fourth, although MFL methods achieve notable performance improvements, they remain **vulnerable to adversarial attacks** (*challenge 4*), potentially limiting their reliability in AI-driven healthcare applications. Even minor adversarial perturbations can result in incorrect predictions directly effecting patient outcomes. Without robust adversarial defenses, such systems may generate unreliable diagnoses, posing serious risks to patient safety.

In this paper, we focus on *addressing cost-effectiveness, information loss in cascaded modules, limited generalization due to restricted modalities, and adversarial vulnerability* – four fundamental challenges in state-of-the-art (SOTA) MFL methods. To address these concerns, we propose two groundbreaking frameworks – **Multi-Attention Integration Learning (MAIL)** and **Robust-MAIL**–jointly redefining AI-driven medical imaging applications. These frameworks achieve *high performance under computational constraints*

while ensuring *reliability against adversarial attacks*, as shown in Figs. 1-2. MAIL tackles the *first three challenges* through two core modules: Efficient Residual Learning Attention (ERLA) and Efficient Multimodal Cross-Attention Module (EMCAM). Specifically, ERLA *addresses challenge 1* by refining multi-scale channel dependencies through low-cost convolutions with channel attention, enhancing representational diversity while preserving computational efficiency (ref. Tables 1-2, 4-5). EMCAM *solves challenges 1-2* by pioneering parallelized fusion of multimodal information across frequency and spatial domains, optimizing performance-efficiency trade-offs while minimizing information loss (ref. Tables 1-2, 6).

Algorithm 1 MAIL Network

```

1: Input:  $m$ -th multimodal input  $x_i \in X = [x_1, x_2, \dots, x_m]$ , where
 $x_{[1:m]} \in \mathbb{R}^{H \times W \times C}$ 
2: Output: Multi-disease tasks (e.g., classification) via two salient
   phases: MSL and TML
3: Procedure:
4: /* MAIL network with the proposed ERLA and EMCAM blocks. Base
   network: ResNet18 */
5: if phase == MSL (Modality-Specific Task Learning) then
6:   for each modality  $i \in [1 : m]$  do
7:     Apply a  $7 \times 7$  convolutional layer as the input layer:
       $x_i \leftarrow \text{Conv}(x_i)$ 
8:   for each filter size in  $\{64, 128, 256, 512\}$  do
9:     Refine multi-scale diverse patterns using ERLA block
       (Eqs. 1–4):
       $x'_i \leftarrow \text{ERLA}(x_i)$ 
10:    Learn enhanced complementary shared representations
        using EMCAM block (Eqs. 5–13):
       $X^S \leftarrow \text{EMCAM}(x'_i)$ 
11:   end for
12:   end for
13: end if
14: if phase == TML (Target-Specific Multitask Learning) then
15:   Perform multi-task learning:
16:    $\mathcal{L}_{\text{TML}} = \sum_{t=1}^T \sum_{m=1}^M \lambda_t^M \cdot \mathcal{L}_t^M(\mathcal{F}(X^S; \beta), Y),$ 
17:    $\beta^* = \arg \min_{\beta} \mathcal{L}_{\text{TML}}$ 
18: end if

```

To *deal with challenge 3*, MAIL learns from and adapts to diverse medical imaging modalities, enhancing its generalizability for multi-disease classification (see Tables 1-2). To *mitigate challenge 4*, we extend MAIL to Robust-MAIL, ensuring reliable predictions under adversarial attacks. We first explore the random projection filter [15] and observe its effectiveness in enhancing MFL robustness (ref. Tables 3-5). Motivated by this, we redesign MAIL into Robust-MAIL by integrating Random Projection with Attention

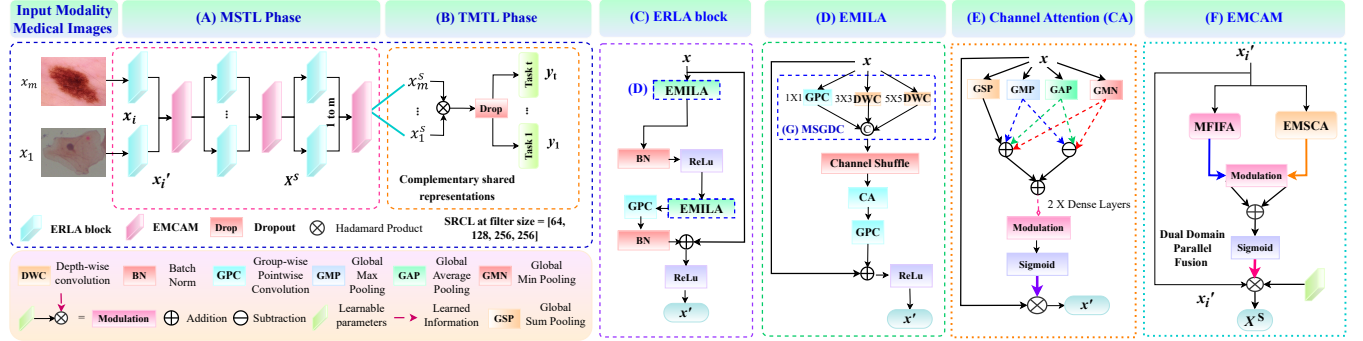


Figure 3: Architecture of MAIL network (comprising of (A) MSLT and (B) TMLT phases). Key components with-in MSLT phase are (C) ERLA and (F) EMCAM blocks. ERLA is based on (D) EMILA module, comprising of (G) MSGDC block inspired from EMCAD’s MSDC [44] and (E) Channel Attention (CA). EMCAM details are in Figure 4.

Noise (RPAN), which combines random projection filtering with modulated attention noise. RPAN *injects stochasticity* into ERLA and EMCAM, disrupting adversarial perturbations while preserving crucial information, transforming MAIL into a robust framework. Our main contributions can be summarized as follows:

- We introduce the MAIL network, designed to enhance MFL’s effectiveness by jointly optimizing frequency and spatial domain information through parallel fusion. This enables effective multi-modal information fusion achieving optimal performance while minimizing computational cost.
- We introduce Robust-MAIL, an extension of MAIL designed for adversarial robustness. It integrates random projection filters with modulated attention noise mechanisms to ensure reliable predictions against adversarial attacks.
- We conduct extensive evaluations against state-of-the-art methods, demonstrating significant improvements across 20 diverse medical imaging datasets.

2 Related Study

Previous works in MFL have been widely explored in natural vision tasks [28, 33, 41, 56], with limited adaptation to medical imaging [7]. For example, MTTU-Net [7] combined CNNs and transformers for glioma segmentation and IDH genotyping but lacked explicit attention mechanisms to learn nuanced multimodal representations. Recent attention-based architectures, including DDA-Net [10], MADGNet [38], NAT [19], POTTER [60], and EMCAD [44], have demonstrated significant advancements in representation learning for both natural and medical imaging tasks. The integration of attention mechanisms into MFL frameworks has played a pivotal role in further enhancing their performance [21, 23–25, 31, 52, 53, 61]. For instance, GLORIA [23] leveraged global-local attention to align radiology reports with images for label-efficient learning. HAMLET [24] and MuMu [25] employed multi-head and lightweight self-attention, respectively, to fuse multimodal sensor data for human activity recognition. In contrast, M³Att [31] used mutual attention to integrate features from dual modalities, enhancing segmentation performance. Similarly, CAF [21] and DRIFA-Net [12] adopted cross-modal and cascaded dual attention for skin cancer diagnosis and multi-disease classification, highlighting the versatility of attention mechanisms. However, as described earlier, current MFL methods

often suffer from computational inefficiency due to computationally intensive convolutions or attentions, potentially risk progressive information loss from cascaded attention transitions, and limited adaptability to learn shared complementary representations effectively. These studies do not utilize the benefits of lightweight multi-scale depth-wise convolutions, parallelized attention fusion to mitigate information loss, and adaptability to diverse medical imaging modalities for enhanced generalizability in multi-disease classification. Therefore, in this work, we propose ERLA and EMCAM, integrated within our MAIL network, to enhance model performance while maintaining computational feasibility – by integrating lightweight multi-scale depth-wise convolutions and parallelized attention mechanism. MFL networks must ensure reliable predictions against adversarial examples, necessitating the development of robust MFL architectures. While several defenses – PNI [22], DBN [18], Learn2Perturb [26], RP filter [15], CAP [57], and CTRW [34] – exist, they primarily focus on adversarial defense in single-modal networks and are often designed for natural images. These approaches overlook the challenges posed by medical imaging, where significant differences in data size, feature characteristics, and task patterns complicate the direct application of natural vision defenses to medical imaging applications [14]. To bridge this gap, we extend MAIL with a random projection filter and modulated attention noise, forming Robust-MAIL to ensure reliable medical AI applications.

3 Proposed Method

Problem Formulation: In this section, let us discuss our proposed multimodal fusion learning network: MAIL, for multimodal image analysis. Given an input $X = [x_1, \dots, x_m]$ from m diverse modalities and labels $Y = [y_1, \dots, y_t]$ for t disease classification tasks, MAIL, denoted as $\mathcal{F}(\cdot)$, aims to learn enhanced complementary shared representations $X^S = [x_1^S, \dots, x_m^S]$ while optimizing $\mathcal{F}(X) \rightarrow Y$ for improved performance with minimal computational cost.

Method Overview: We provide a holistic overview of our proposed MAIL network, as shown in Fig. 3 (A, B). *Detailed steps of MAIL are provided in Algorithm 1.* We will show how MAIL utilizes information fusion learning with efficient attention strategies, ensuring adaptability across diverse neural architectures while maintaining optimal performance with minimal computational overhead. It comprises of two salient phases: *Modality-Specific Task Learning*

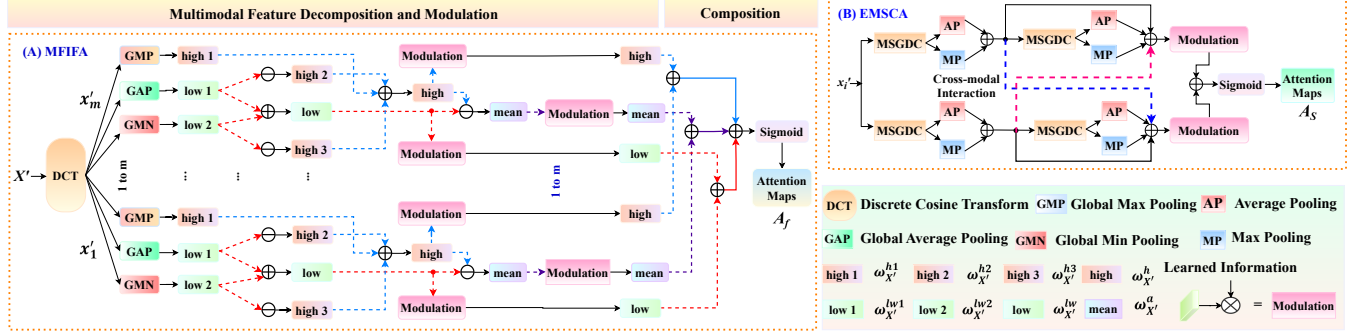


Figure 4: Components of EMCAM: (A) MFIFA module captures multi-frequency multimodal global contexts, while (B) EMSCA module refines multimodal spatial representations.

(MSTL) and Target-Specific Multitask Learning (TMTL). MSTL captures enhanced complementary shared representations, while TMTL enables multi-task learning for disease classification. We describe these two salient phases, as well as random projection with attention noise mechanism in the following sections.

3.1 Modality-Specific Task Learning Phase

MSTL consists of m modality-specific branches and incorporates two key blocks as follows:

- Efficient Residual Learning Attention (ERLA) block (Fig. 3) effectively learns refined multi-scaled diverse patterns – $X' = [x'_1, \dots, x'_m] \in \text{ERLA}(\cdot)$ for each modality-specific network branch.
- Efficient Multimodal Cross Attention Module (EMCAM) block (Figs. 3–4), which takes $x'_{[1:m]}$ from each network branch as input to learn enhanced complementary shared representations X^S .

3.1.1 Efficient Residual Learning Attention Block (ERLA). ERLA block (ref. Fig. 3(C)) is an extension of the Multi-Scale Convolution Block (MSCB) from EMCAD [44] as it is enhanced with our novel Efficient Multi-scale Information Learning Attention (EMILA) module (ref. Fig. 3(D)). Our ERLA block integrates EMILA, ReLU (R(.)), batch normalization (BN(.)), and a 1×1 group-point-wise convolution (GPC(.)). Given input x , the ERLA recursively refines multi-scale representations via skip connections, enabling progressive updates to x for improved regularization:

$$\text{ERLA}(x) = \text{R}(x + \text{BN}(\text{GPC}(\text{EMILA}(\text{R}(\text{BN}(\text{EMILA}(x))))))). \quad (1)$$

Let us discuss EMILA in the following. EMILA (ref. Fig. 3 (D)) is inspired by EMCAD's MSDC [44] but introduces a key enhancement: channel attention. It consists of three components: a) a multi-scale group with depth-wise convolutions (MSGDC) block (ref. Fig. 3(G)), b) channel shuffle [44], and c) channel attention to learn enhanced multi-scale representations. Let us discuss MSGDC block first. Our MSGDC block consists of three parallel branches: the first branch employs a GPC(.) layer, while the other two utilize multi-scale depth-wise convolutions (DWC_k(.)) at multiple scales $k \in \{3 \times 3, 5 \times 5\}$. These branches extract diverse patterns, which are then fused to capture multi-scale spatial details as $x' = \text{MSGDC}(x)$:

$$\text{MSGDC}(x) = \theta(\forall_{k \in \{3 \times 3, 5 \times 5\}}, \text{DWC}_k(x), \text{GPC}(x)). \quad (2)$$

Since depth-wise convolutions overlook relationships among channels, in EMILA, channel shuffle is utilized to shuffle channels across groups to incorporate relationships among channels [44]. Therefore,

final EMILA module can be formulated as:

$$\text{EMILA}(x') = x + \text{GPC}(\text{CA}(\text{MSGDC}(x))). \quad (3)$$

Let us in the following explain the channel attention (CA(.)) block. The output of MSGDC block is used as input to CA block (ref. Fig. 3(E)). The block is motivated to *refine modality-specific* representations, that first incorporates multi-perspective pooling operations – global average pooling (GAP(.)), global max pooling (GMP(.)), and global min pooling (GMN(.)) to capture diverse channel dependencies. The resulting contexts undergo fusion (addition and subtraction followed by addition) to enhance channel diversity and compressed through two fully connected layers ($f(\cdot)$). A modulation process adaptively scales informative channels using learnable parameters (ϑ_x), followed by a sigmoid activation ($\sigma(\cdot)$) to generate channel attention maps (A_c). These maps dynamically recalibrate the input x through element-wise multiplication, yielding refined representations ($x_c = \text{CA}(x')$) for each modality m (ref. Eq. 4). Next, GPC(.) restores the original number of channels while encoding inter-channel dependencies. A skip connection recursively updates x with refined representations, further enhancing regularization. We formalize our CA block as:

$$\text{CA}(x') = x' \times \sigma\left(f\left(\left[\sum_{p=1}^3 G_p(x')\right] + [\mu]\right) \times \vartheta_x\right), \quad (4)$$

where $G_p \in [\text{GMP}, \text{GAP}, \text{GMN}]$ and $\mu \in \text{GMP}(x') - \text{GAP}(x') - \text{GMN}(x')$.

3.1.2 Efficient Multimodal Cross Attention Module (EMCAM). In this section, we discuss our proposed EMCAM block (ref. Fig. 3(F), and Fig. 4), which aims to learn enhanced complementary shared representations X^S by refining the input $X' = [x'_1, \dots, x'_m]$ obtained from the ERLA block. Here, $x'_{i \in [1:m]} \in \mathbb{R}^{H \times W \times C}$ represents the i -th component of m input modalities, where H , W , and C denote height, width, and channels dimensions, respectively. By integrating global frequency-domain contexts with fine-grained spatial details, EMCAM enhances the model's ability to capture a broader range of dependencies across frequency and spatial domains. This facilitates effective multimodal fusion, leading to a richer understanding of multimodal images. To achieve this, EMCAM integrates two parallel attention module:

- Multimodal Frequency-domain Information Fusion Attention (MFIFA) (ref. Fig. 4 (A)) – for capturing multi-frequency multimodal global contexts.

- Efficient Multimodal Spatial-domain Cross Attention (EMSCA) (Fig. 4 (B)) – for refining multimodal spatial details with minimal cost.

Algorithm 2 : Adversarial Training with RPAN

```

1: Require:
2: Robust-MAIL network  $\mathcal{F}(\cdot)$  with learning parameter  $\beta$ ;
3: Number of random projection filters for RPAN layer  $N_{r_\xi}$ ;
4: Weight decay for RPF  $\varrho$ ;
5: Number of RPAN layers  $\tau_{E/b}$  across the  $E$ -th total number of ERLA and
   EMCAM blocks and  $b$ -th branches;
6: CA ( $\zeta$ ), EMSCA ( $\zeta$ ), MFIFA ( $\Gamma$ ), and modulated attention noise ( $\eta'_l$ );
7: Perturbation size  $\epsilon$ ;
8: Attack step size  $a$ ;
9: Number of attack iterations  $k$ ;
10: Training set  $\{X \in x_i, Y = \{y_1, \dots, y_t\}\}$ ;
11: Procedure:
12: while not converged do
13:   Sample a batch  $\{bX, bY\}_{i=1}^n$  from  $\{X, Y\}$ ;
14:   Apply RPFs for Attack phase:
15:   for  $j = 1$  to  $N_r$  do
16:     Initialize random filters  $\mathcal{R}_j \sim \mathcal{N}(0, r^2)$ , where  $r \in \sigma$ ;
17:   end for
18:   Apply RPAN Layers for Attack phase:
19:   for each  $E/b$  do
20:     Compute RPAN to learn enhanced noisy features:
21:      $\tau(X) = bX \times \left( \sum_{\Phi \in \{\Gamma, \zeta\}} \Phi \left( \zeta \left( (\mathcal{R}_{1:N_{r_\xi}} * bX) \times \eta'_l \right) * \mathcal{R}_{1:N_{r_\xi}} \right) \times \eta'_l \right)$ 
22:      $\min_{\beta} \max_{X^*} \left( \mathcal{L}_{\text{MTL}}(\mathcal{F}(X^*, \beta), Y) + \varrho (\|\mathcal{R}_{N_r+1:N}\| + \|\tau_{1:E/b}\|) \right)$ 
23:     s.t.  $\|X^* - X\| \leq \epsilon$ 
24:     where  $*$  denotes convolution.
25:   end for
26:   Generate Adversarial Examples:
27:   Randomly initialize adversarial perturbation  $\delta$ ;
28:   for  $i = 1$  to  $k$  do
29:      $\delta \leftarrow \delta + a \cdot \text{sign}(\nabla_{bX} \mathcal{L}_{\text{MTL}}(\mathcal{F}_\beta(bX^*), bY))$ 
30:      $bX^* \leftarrow \text{Clip}_{bX}^\epsilon(bX + \delta)$ 
31:   end for
32:   Apply RPAN integrated by RPFs and modulated attention noise
   for Inference phase:
33:   for each  $E/b$  do
34:     for  $j = 1$  to  $N_r$  do
35:       Initialize random filters  $\mathcal{R}_j \sim \mathcal{N}(0, r^2)$ ;
36:        $\tau(X) = bX \times \left( \sum_{\Phi \in \{\Gamma, \zeta\}} \Phi \left( \zeta \left( (\mathcal{R}_{1:N_{r_\xi}} * bX) \times \eta'_l \right) * \mathcal{R}_{1:N_{r_\xi}} \right) \times \eta'_l \right)$ 
37:        $\min_{\beta[I]} \max_{X^*} \left( \mathcal{L}_{\text{MTL}}(\mathcal{F}(X^*, \beta[A]), Y) + \varrho (\|\mathcal{R}_{N_r+1:N}\| + \|\tau_{1:E/b}\|) \right)$ 
38:       s.t.  $\|X^* - X\| \leq \epsilon$ 
39:     end for
40:   end for
41:   Adversarial Training Optimization:
42:    $\beta = \beta - \nabla_\beta \left( \mathcal{L}_{\text{MTL}}(\mathcal{F}(X^*, \beta), Y) + \varrho \left( \|\mathcal{R}_{N_r+1:N}\| + \|\tau_{1:E/b}\| \right) \right)$ 
43: end while
  
```

The outputs of these blocks are fused and normalized via a sigmoid activation ($\sigma(\cdot)$) to generate multimodal attention maps A_m .

These maps adaptively recalibrate X' through element-wise multiplication and channel-wise trainable parameters $\vartheta_m \in \mathbb{R}^C$, which dynamically weights modality-specific contributions. The enhanced shared representation X^S is computed as:

$$X^S = X' \times A_m \times \vartheta_m. \quad (5)$$

The parallel design of MFIFA and EMSCA blocks allows EMCAM to *jointly optimize global frequency contexts and spatial dependencies while maintaining computational efficiency*. The following sections provide a detailed discussion of these attention modules.

A. Multimodal Frequency-domain Information Fusion Attention (MFIFA) module is designed to learn multi-frequency multimodal global contexts, denoted as $\omega_{X^e}^{mf}$, by analyzing frequency-based relationships to facilitate seamless feature alignment across modalities through the reformulation of the input X' . MFIFA is illustrated in Fig. 4 (A) and consists of three stages:

Stage 1: Multimodal Feature Decomposition – Given input X' from the ERLA block, it first applies the discrete cosine transform (DCT) to convert spatial representations into frequency-domain information. These contexts are then decomposed into diverse frequency segments – low, high, and mean – by applying three global pooling operations – GMN(.), GAP(.), and GMP(.) – across m modalities:

- To capture diverse low-frequency components $\omega_{X'}^{lw}$, it applies two global pooling operations – GMN(.) and GAP(.) – to X' , obtaining low frequencies – $\omega_{X'}^{lw1}$ and $\omega_{X'}^{lw2}$, which are then fused to form the diverse low-frequency component i.e. $\omega_{X'}^{lw}$:

$$\omega_{X'}^{lw1} = \text{GMN}(X') \quad \text{and} \quad \omega_{X'}^{lw2} = \text{GAP}(X'), \quad \text{then} \quad \omega_{X'}^{lw} = \omega_{X'}^{lw1} + \omega_{X'}^{lw2}. \quad (6)$$

- To capture diverse high-frequency components i.e., $\omega_{X'}^h$, it computes the residuals by subtracting the low-frequency terms from X' , yielding high frequencies – $\omega_{X'}^{h1}$ and $\omega_{X'}^{h2}$. Additionally, we apply (.) on X' to learn another high frequency: $\omega_{X'}^{h3}$. These high frequencies are fused to form high-frequency component i.e., $\omega_{X'}^h$ as:

$$\omega_{X'}^{h1} = X' - \omega_{X'}^{lw1}, \quad \omega_{X'}^{h2} = X' - \omega_{X'}^{lw2}, \quad \omega_{X'}^{h3} = \text{GMP}(X'). \quad (7)$$

- The mean-frequency component i.e., $\omega_{X'}^a$ is obtained by computing the difference between the high- and low-frequency components: $\omega_{X'}^h$ and $\omega_{X'}^{lw}$:

$$\omega_{X'}^h = \omega_{X'}^{h1} + \omega_{X'}^{h2} + \omega_{X'}^{h3}, \quad \omega_{X'}^a = \omega_{X'}^h - \omega_{X'}^{lw}. \quad (8)$$

Stage 2: Modulation – The resulting frequency components – $(\omega_{X'}^h, \omega_{X'}^{lw}, \omega_{X'}^a)$ – are modulated via learnable parameters α_m , φ_m , and γ_m through element-wise multiplication. This adaptively re-weights their contributions based on modality-specific importance.

Stage 3: Composition – The resulting components are fused across modalities to learn multi-frequency global contexts, denoted as $\omega_{X'}^{mf}$. Specifically, for each modality branch input (e.g., $x'_i \in X'$), the corresponding low-, high-, and mean-frequency components are hierarchically fused with those from other modality branches (e.g., x'_j for $j \in [m]$). Finally, these components undergo further fusion to capture these global contexts, followed by a sigmoid activation (σ) to

generate the frequency-domain attention map ($A_f = \text{MFIFA}(X')$):

$$A_f = \sigma \left(\sum_{i=1}^m \left(\alpha_i \times \omega_{x_i}^{lw} + \varphi_i \times \omega_{x_i}^h + \gamma_i \times \omega_{x_i}^a \right) \right). \quad (9)$$

B. Efficient Multimodal Spatial-domain Cross Attention (EMSCA) module is designed (ref. Fig. 4 (B)) to efficiently capture multimodal spatial details through multi-scale representations and cross-modal attention. In particular, EMSCA leverages MSGDC from the EMILA module. As, 1×1 point-wise/depth-wise convolutions lacks spatial awareness and scale diversity, MSGDC block in EMSCA leverages multiple scales (e.g., $3 \times 3, 5 \times 5$) within grouped channels to capture multi-scale spatial contexts at minimal computational cost. For each modality branch input $x'_i \in X'$ where $i \in [1, m]$, it computes:

$$S(x'_i) = \text{AP}(\text{MSGDC}(x'_i)) + \text{MP}(\text{MSGDC}(x'_i)), \quad (10)$$

where average pooling (AP) and max pooling (MP) learn complementary spatial details. These learned patterns are fused recursively to progressively compress spatial dimensions, forming a *hierarchical spatial refinement* as:

$$\text{MSGDC}(x'_i) \xrightarrow{\text{AP/MP}} \theta \xrightarrow{\text{fusion}} S(S(x'_i)). \quad (11)$$

To enable **cross-modal interaction**, EMSCA employs symmetric skip connections between paired modalities (x'_i and its counterpart x'_{m-i+1}) to fuse base multimodal spatial representations ($S(x'_i)$ and $S(x'_{m-i+1})$) along with hierarchical representations ($S(S(x'_i))$), thereby learning cross-modal spatial contexts. This bidirectional interaction also enhances modality-specific regularization through recursive hierarchical compression. The learned spatial contexts are then adaptively modulated using learnable parameters ϑ_i , dynamically scaling each modality pair's contributions. Finally, feature fusion (addition) integrates the refined spatial details into the multimodal spatial context, followed by a sigmoid activation to generate spatial-domain attention map $A_s = \text{EMSCA}(\cdot)$:

$$\text{EMSCA}(X') = \sum_{i=1}^m \vartheta_i \times \left(\underbrace{S(x'_i) + S(x'_{m-i+1})}_{\text{cross-modal interaction}} + \underbrace{S(S(x'_i))}_{\text{hierarchical representation}} \right). \quad (12)$$

Finally, to fuse the contributions of the MFIFA and EMSCA modules, we compute the final attention map A_m by adaptively scaling their outputs using learnable parameters ϑ_f and ϑ_s . These parameters dynamically balance the relative importance of the two modules, enhancing overall performance. The attention map is computed as:

$$A_m = \sigma(\vartheta_f \times \text{MFIFA}(X') + \vartheta_s \times \text{EMSCA}(X')). \quad (13)$$

3.2 Target-specific Multitask Learning

The TMTL phase of MAIL network uses shared representations X^S from MSLT phase for multi-disease classification across m modalities. It maps the input X^S to task predictions Y through the loss function $\mathcal{L}_{\text{TMTL}}$, where λ_t^m balances task-modality-specific losses \mathcal{L}_t^m . The optimal model parameters β^* are learned by minimizing $\mathcal{L}_{\text{TMTL}}$:

$$\mathcal{L}_{\text{TMTL}} = \sum_{t=1}^T \sum_{m=1}^M \lambda_t^m \mathcal{L}_t^m(\mathcal{F}(X^S; \beta), Y), \quad \beta^* = \arg \min_{\beta} \mathcal{L}_{\text{TMTL}}. \quad (14)$$

where β signifies the MAIL parameters.

3.3 Random Projection with Attention Noise

Adversarial examples $X^* = X + \delta$, generated by perturbing inputs X with bounded noise δ , compromise the reliability of the MAIL network by maximizing the loss $\mathcal{L}_{\text{TMTL}}$. This causes misclassifications through the network's predictions via $\mathcal{F}(X^*; \beta)$, where δ represents

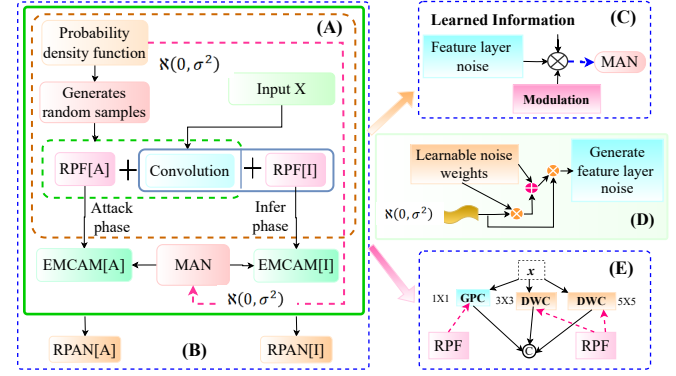


Figure 5: (A-B) Overview of Robust-MAIL, where MAIL integrates EMCAM, incorporating RPF and MAN to form the RPAN module. RPAN consists of key components: RPF[A] / RPF[I] (sampled Gaussian matrices), EMCAM[A] / EMCAM[I], and RPAN[A] / RPAN[I], where [A] and [I] denote attack and inference phases. (C-D) Illustration of MAN utilizing learnable feature-layer noise, where noise is modulated through learnable weights combined with random noise to enhance robustness. (E) Integration of RPF into the MSGDC from ERLA and EMCAM.

adversarial perturbations constrained by $\|\delta\|_\infty \leq \epsilon$. The adversarial objective for modality m is formalized as:

$$\max_{X^*} \mathbb{E}_{(X, Y) \sim \mathcal{D}_m} (\mathcal{L}_{\text{TMTL}}(\mathcal{F}(X^*; \beta), Y)) \quad \text{s.t.} \quad \|X^* - X\|_\infty \leq \epsilon, \quad (15)$$

where \mathcal{D}_m denotes the data distribution for modality m . To ensure adversarial robustness in the MAIL network, we propose Robust-MAIL, an enhanced architecture incorporating *Random Projection with Attention Noise* (RPAN) module (ref. Fig. 5). The RPAN module incorporates two key blocks within EMCAM block, described in the following:

- **Random Projection Filter (RPF):** Replaces conventional convolution filters in the depthwise (DWC) and point-wise (GPC) convolutions in ERLA and EMCAM, with randomly sampled Gaussian matrices (ref. Figs. 5 (A, E)). This introduces stochasticity into feature transformations, disrupting adversarial pattern propagation.
- **Modulated Attention Noise (MAN):** Injects dynamically scaled learnable feature layer noise into EMCAM's attention maps during modulation at training and inference (ref. Figs. 5 (A-D)). This adaptively corrupts adversarial gradients while smoothing learned representations.

A. Random Projection Filter (RPF): For a convolution layer with N filters $\mathcal{R}_1, \dots, \mathcal{R}_N$, we partition them into two groups: (i) static randomly sampled RPFs ($\mathcal{R}_1, \dots, \mathcal{R}_{N_r} \sim \eta(0, \sigma^2)$) and (ii) trainable convolution filters ($\mathcal{R}_{N_r+1}, \dots, \mathcal{R}_N$) used in conventional, depthwise, and pointwise convolutions. These filters, with kernel size r , are applied to the input X . Unlike prior works [15], our approach uniquely integrates randomness across both depth-wise and group-point-wise convolutions in ERLA and EMCAM blocks (see Figure 5(E)).

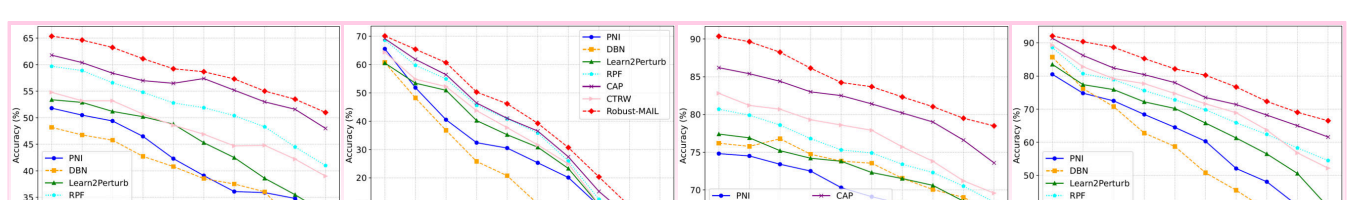
Concurrently, modulated attention noise generates diverse noise patterns X^Z , thereby further disrupting the generation of effective adversarial perturbations. Note that we use terms [A] and [I] to make explicit use of RPAN, RPF, and EMCAM in the attack

Table 1: Performance comparison of MAIL with existing methods (M1–M10) on D1–D10 datasets for classification. Bold and red indicate the best and second-best results, respectively. MAIL employs ResNet18 and ResNet50 as base networks, denoted as MAIL–RN18 and MAIL–RN50.

Datasets →	D1: Nickparvar			D2: IQ-OTHNCCD			D3: Tuberculosis			D4: BCCD			D5: HAM10000			D6: SIPaKMeD			D7: CRC			D8: CNMC-2019			D9: KVASIR			D10: CBIS-DDSM			Cost Analysis	
Models ↓	ACC	F1	AUC	ACC	F1	AUC	ACC	F1	AUC	ACC	F1	AUC	ACC	F1	AUC	ACC	F1	AUC	ACC	F1	AUC	ACC	F1	AUC	ACC	F1	AUC	Params	Flops			
DDA-Net	96.8	96.6	97.1	98.1	97.4	98.1	98.6	97.7	98.8	98.2	98.2	98.6	92.2	91.8	92.6	92.5	92.8	91.9	93.4	92.7	93.6	92.6	91.8	93.1	90.6	90.2	91.1	92.5	91.8	91.5	12.1	1.12
NAT	95.5	95.5	96.6	97.5	97.3	97.2	98.4	96.7	98.2	98.1	97.7	98	93.1	92.6	93.3	91.1	91.1	91.5	96.8	96.7	98	94.1	93.7	93.4	89.3	87.6	90.1	92.0	91.7	91.9	20	1.1
POTTER	95.1	94.7	94.7	97.2	96.5	97.2	97.8	97.2	98.2	96.4	96.1	91.3	91.1	91.8	92.3	92.1	92.3	95.8	95.2	96.2	93.8	93.5	92.7	91.5	90.7	90.9	91.3	91.1	90.8	12	0.95	
MFMSA	98.3	98.0	98.4	99.5	99.3	99.5	98.9	97.4	98.6	98.3	98.5	98.8	97.9	97.3	94.7	94.4	95.3	97.3	97.3	97.6	96.2	96.0	96.3	90.9	90.5	90.7	94.6	94.5	94.6	26.9	1.4	
Gloria	98.1	97.5	97.9	98.5	98.3	98.5	98.2	97.5	98.9	98.1	97.6	98.4	93.7	93.7	94.5	94.2	94.2	94.2	96.2	95.5	95.9	93.7	93.5	93.2	89.6	89.1	90.2	92.5	91.2	91.9	30.8	1.54
MTT-Net	97.9	98.0	98.0	99.5	99.2	99.5	98.8	97.4	99	97.8	97.6	98.2	97.4	96.5	97.1	91.9	92.3	92.5	97.3	96.4	97.5	94.3	93.6	94.2	91.2	90.8	91.0	94.1	93.3	94.5	38.1	6.8
HAMLET	96.2	95.9	96.2	98	97.5	97.5	97.1	97.1	97.5	97.2	97.8	93.5	93.4	93.2	92.8	92.8	93	96.7	96.3	97.2	92.9	92.2	93.4	89.3	87.4	88.6	91.8	91.8	91.3	57.3	3.52	
MuMu	96.8	96.8	97.1	98.2	97.9	98.7	97.8	97.3	97.8	97.5	97.8	92.3	93.1	92.3	91.7	92.8	96.8	96.3	96.8	93.3	92.7	93.8	88.4	87.3	88.1	92.1	91.7	92.5	56.6	2.97		
M ³ Att	97.5	97.5	97.9	98.8	98.8	98.8	98.5	97.2	98.8	98.3	98	98.5	95.5	94.8	95.2	92.2	91.4	92.3	95.5	95.2	95.1	93.9	93.1	94.2	90.9	90.5	91.2	93.2	92.7	93.6	183	12.14
DRIFA-Net	98.4	98.4	98.7	99.7	99.5	99.5	99.1	97.4	99.1	98.9	98.8	98.9	98.2	97.9	98.5	95.6	95.5	95.9	97.5	97.2	96.7	95.9	95.8	96.3	91.9	91.1	91.7	95.2	95	94.5	53.8	4.83
MAIL–RN18	98.8	98.6	98.9	99.7	99.5	99.7	99.3	97.8	99.3	99.1	99.1	99.9	99.4	99.4	99.7	96.3	96.3	96.5	98.4	97.9	98	97.1	96.8	97.6	92.3	91.6	96.1	96.1	11.7	1.84		
MAIL–RN50	99.2	99.1	99.2	99.7	99.5	99.5	99.5	98.1	99.4	99.3	99.6	99.8	98.1	98.1	98.9	98.7	98.3	98.7	97.3	97.1	97.8	92.7	92.2	93.5	96.5	96.5	96.9	20.8	2.18			

Table 2: Performance comparison of MAIL with existing methods (M1–M10) on D11–D16 (classification) and (M11–M21) on D17–D20 (segmentation). Bold indicates the best result. MAIL employs MobileNetV2, ResNet18, and SegNet as base networks, denoted as MAIL–M2, MAIL–RN18, and MAIL–Seg.

Datasets →	D11: PathMNIST			D12: PneumoniaMNIST			D13: RetinaMNIST			D14: BreastMNIST			D15: TissueMNIST			D16: OrganMNIST			D17: KVASIR			D18: ISIC 2018			D19: BraTs 2020			D20: LiTs			Params	Flops
Models ↓	ACC	AUC	ACC	ACC	AUC	ACC	ACC	AUC	ACC	ACC	AUC	ACC	ACC	AUC	ACC	ACC	AUC	Models ↓	DICE	mIOU	DICE	mIOU	DICE	mIOU	DICE	mIOU	DICE	mIOU	Params	Flops		
DDA-Net	92.25	99.84	90.25	97.25	67.62	78.46	86.35	90.18	68.90	94.54	95.75	99.80	UNet	80.55	72.60	87.32	80.24	81.79	76.54	88.80	84.64	34.5	65.5									
NAT	91.80	99.78	89.95	97.12	66.58	77.60	86.24	90.10	68.42	94.39	95.70	99.80	UNet++	84.37	77.48	87.30	80.25	82.55	76.37	89.45	85.08	9.2	34.7									
POTTER	91.45	99.50	89.89	97.74	63.54	74.26	87.15	90.90	67.98	93.29	96.06	99.85	AttnUNet	83.89	77.15	87.80	80.54	82.78	76.48	86.72	84.98	34.9	66.6									
MFMSA	92.28	99.70	91.49	98.15	69.10	78.84	88.90	93.37	72.45	95.29	96.12	99.90	PolyPVT	91.67	85.90	90.42	83.85	86.38	79.50	93.83	88.20	25.1	5.3									
Gloria	91.94	99.78	91.25	97.88	66.89	77.55	87.52	91.07	69.88	94.72	95.68	99.80	TransUNet	86.45	81.37	87.28	81.20	84.90	78.24	92.12	87.85	105	38.5									
MTT-Net	92.28	99.34	90.47	97.79	61.75	75.59	87.57	90.86	69.10	93.75	95.63	99.85	SwinUNet	88.50	82.74	87.77	81.93	85.56	78.80	93.90	88.32	27.2	6.2									
HAMLET	91.85	99.29	89.42	97.65	63.38	75.81	86.88	90.48	69.58	93.98	95.28	99.80	TransFuse	88.95	83.50	89.14	82.31	83.80	77.25	91.34	86.25	143	8.27									
MuMu	92.12	99.56	89.84	97.75	64.28	77.41	86.75	90.67	69.75	94.19	95.49	99.80	MTTU-Net	86.51	81.70	89.22	82.58	84.82	78.12	90.45	85.21	71.6	20.9									
M ³ Att	91.72	99.15	91.25	97.82	63.15	76.90	87.84	91.55	70.54	94.52	94.52	99.85	MADGNet	90.77	85.38	90.20	83.76	90.18	81.32	94.35	89.14	31	14.2									
MAIL–M2	93.10	99.75	91.83	98.24	69.38	79.81	88.95	93.67	73.75	96.03	96.45	99.90	DRIFA-Net	90.90	86.14	90.55	83.87	89.92	81.25	94.50	89.82	67.3	19.94									
MAIL–M3	93.25	99.84	92.05	98.60	69.45	80.54	89.65	93.80	74.18	96.79	96.79	99.90	EMCAD	92.84	86.45	90.91	84.12	90.53	82.55	94.57	89.82	26.8	5.6									
MAIL–RN18	93.73	99.95	92.49	98.83	70.69	81.32	90.06	93.92	74.84	96.56	97.07	99.94	MAIL–Seg	93.05	86.50	91.27	84.46	91.13	82.78	95.16	80.27	12.58	7.89									

**Figure 6: Evaluation of Robust-MAIL's performance against stronger PGD attacks on the D5 and D3 datasets.**

and inference phases, respectively (ref. Figs. 5 (A–B)). By introducing stochasticity at both input and feature levels, RPF within Robust-MAIL significantly enhances adversarial defense.

B. Modulated Attention Noise. MAN block is designed by injecting random learnable feature layer noise (η'_i) (ref. Fig. 5 (D)) (alongside RPFs where applicable) into: a) CA(\cdot) represented as (ζ), b) MFIFA(\cdot) represented as (Γ) and c) EMSCA(\cdot) represented as (ζ), during their respective modulation processes. This enhances the

learning of diverse noisy representations X^Z , enhancing the adversarial robustness of the MAIL network. *Additional details are provided in the Appendix A and Appendix B.*

For adversarial robustness, RPAN is applied across E/b trainable convolution layers, where E is the total number of ERLA and EMCAM blocks and b indexes modality-specific branches (e.g., $b = 2$). RPFs apply across N_{r_ξ} -th trainable layers in each (E/b), with N_{r_ξ} denoting the total trainable convolutional layers per EMCAM module (ξ). The output enhanced noisy representations X^Z via the RPAN layer

Table 4: Performance comparison of ERLA, MFIFA, and EMSCA modules in MAIL on benchmark datasets D5 and D6.

Dataset		ERLA	MFIFA	EMSCA	Acc	F1	Params	Dataset		ERLA	MFIFA	EMSCA	Acc	F1	Params
D5	+	×	×	×	94.9	94.7	23.4	D6	+	×	×	90.1	88.9	23.4	
	+	×	×	✓	96.5	96.5	23.7		+	×	✓	91.9	91.4	23.7	
	+	✓	✓	×	96.9	96.8	23.9		+	✓	✓	92.3	92.3	23.9	
	✓	✓	✓	✓	98.9	98.8	24.2		+	✓	✓	95.8	95.6	24.2	
	✓	✓	×	×	95.9	95.6	9.83		✓	✓	×	91.5	91.2	9.83	
	✓	✓	✓	✓	97.7	97.7	10.2		✓	✓	✓	93.6	93.4	10.2	
	✓	✓	✓	✓	98.1	98.1	10.4		✓	✓	✓	94.5	94.5	10.4	
		✓	✓	✓	99.4	99.4	11.7			✓	✓	✓	96.3	96.3	11.7

Table 5: Evaluation of EMILA components (MSGDC and CA), MFIFA components (CO and DF), and EMSCA components (MSGDC and CMI) (ref. section 4.3) on D5 and D6 datasets. For Robust-MAIL, we assess the RPAN components: RPF and MAN, along with utilizing RPF@E on the D5 and D3 datasets. "+" and "++" denote evaluations for MAIL and Robust-MAIL.

	EMILA		MFIFA		EMSCA		D5		D6		Robust-MAIL			D5		D3	
	MSGDC	CA	MO	DF	MSGDC	CMI	Acc	Acc	Params	RPF@E	RPF	MAN	Acc	Acc	Acc	Acc	
+	+	+	+	+	+	+	94.9	90.1	23.4	+	+	+	0	2.58			
	✓	✓	✓	✓	✓	✓	96.49	92.15	9.85	✓	✓	✓	18.37	25.42			
	+	✓	✓	✓	✓	✓	97.78	94.79	24.2	+	+	✓	48.27	73.39			
	✓	✓	✓	✓	✓	✓	97.42	93.90	10.4	+	✓	✓	46.95	70.44			
	✓	✓	✓	✓	✓	✓	98.48	95.52	10.8	*	+	✓	61.18	82.56			
	✓	✓	✓	✓	✓	✓	97.51	94.47	10.2	—	—	—					
	✓	✓	✓	✓	✓	✓	97.90	94.76	10.2	✓	✓	✓	63.29	86.50			
		✓	✓	✓	✓	✓	99.40	96.31	11.7	✓	✓	✓	60.65	82.24			

$\tau(\cdot)$, for each E :

$$\tau(X) = X \times \left(\sum_{\Phi \in \{\Gamma, \zeta\}} \Phi \left(\zeta \left((\mathcal{R}_{1:N_{r_\zeta}} * X) \times \eta'_l \right) \times \mathcal{R}_{1:N_{r_\zeta}} \right) \times \eta'_l \right). \quad (16)$$

The objective function for adversarial robustness in Robust-MAIL can be reformulated as:

$$\min_{\beta} \max_{X^*} \left(\mathcal{L}_{\text{TMTL}}(\mathcal{F}(X^*, \beta), Y) + \varrho(\|\mathcal{R}_{N_r+1:N}\| + \|\tau_{1:E/b}\|) \right) \text{ s.t. } \|X^* - X\| \leq \epsilon. \quad (17)$$

where ϱ denotes the hyperparameters of weight decay.

3.3.1 Adversarial Training with RPAN. White-box attacks can efficiently craft perturbations δ for a fixed network $\mathcal{F}(\cdot)$ via gradient ascent. However, it is difficult for the generated adversarial example $X^* \in X + \delta$ to successfully attack another network $\mathcal{F}'(\cdot)$ [15]. Following the RPF method, we generate adversarial examples using RPAN, denoted as $\tau_{1:E/b}[A]$ during the attack phase. These examples are then applied in adversarial training, where the RPAN layer $\tau_{1:E/b}[I]$ is employed during inference (Fig. 5). This setup reformulates the min-max optimization in Eq. 17 as:

$$\min_{\beta} \max_{X^*} \left(\mathcal{L}_{\text{TMTL}}(\mathcal{F}(X^*, \beta[A]), Y) + \varrho(\|\mathcal{R}_{N_r+1:N}\| + \|\tau_{1:E/b}\|) \right). \quad (18)$$

Adversarial training with RPAN (ref. Algorithm 2) enhances Robust-MAIL's adversarial robustness. In white-box scenarios where attackers have access to RPAN parameters $\tau_{1:E/b}[A]$, adversarial examples X^* are generated with respect to $\mathcal{F}(X^*, \beta[A])$. However, during evaluation, noise is regenerated by $\tau_{1:E/b}[I]$, making X^* less vulnerable to $\mathcal{F}(X^*, \beta[I])$ and thus enhancing robustness against these attacks.

4 Experimental Analysis and Results

Datasets – We utilized 20 medical imaging datasets: D1–D10 include [39], [1], [45], [51], [54], [42], [29], [37], [43], and [49]; D11–D16 are from MedMNIST; D17–D20 comprise [36], [4], [27], and [8]. All

Table 6: Performance comparison of cascaded attention (CAT) and parallel fusion attention (PFA) within our MAIL on D5 and D6 datasets.

Dataset	PFA	CAT	Acc	F1	Dataset	PFA	CAT	Acc	F1	Params
D5	✗	✓	99.1	99.0	D6	✗	✓	95.9	95.9	11.7

images are resized to $128 \times 128 \times 3$ (for classification) and $224 \times 224 \times 3$ (for segmentation) with an 80%/10%/10% train/val/test split (*when applicable*) and standard augmentation applied. *Dataset descriptions are provided in the Appendix C.*

Data Preprocessing. We augment each training image with three image-level transforms—rotation (20°), translation (5 px in both axes), and 3×3 Gaussian blur—producing three additional variants per sample. All augmented images inherit the original label. We then concatenate the augmented set with the original data (yielding a 4× larger training set) and randomly shuffle the combined dataset to improve training diversity. These augmentations encourage robustness to common medical imaging variations in pose, spatial alignment, and acquisition noise.

Models: We evaluate MAIL against state-of-the-art (SOTA) single-modal learning and MFL networks across 16 classification and 4 segmentation datasets, with Robust-MAIL tested on 8 datasets for adversarial robustness. For classification, single-modal learning networks include DDA, NAT, POTTER, and MFMFA of MADGNet [38] (denoted as M1–M4) respectively, while MFL networks – such as Gloria [23], MTTU-Net [7], HAMLET [24], MuMu [25], M³Att, and DRIFA-Net [12] – are reconfigured to match our MFL network (denoted as M5–M10) respectively. For segmentation, we evaluate MTTU-Net and DRIFA-Net alongside SOTA models, including UNet [47], UNet++ [62], AttnUNet [40], PolypPVT [13], TransUNet [6], SwinUNet [5], TransFuse [59], MADGNet [38], and EMCAD [44] (denoted as M11–M21) respectively. To assess adversarial robustness, we integrate methods like PNI, DBN, Learn2Perturb, RPF, CAP, and CTRW into MAIL (denoted as M22–M27) respectively. For classification (D1–D16), we use ResNet18 [20], ResNet50 [20], and MobileNetV2 [48] as backbones, while SegNet [3] is used for segmentation (D17–D20).

Notation – Accuracy (Acc), F1 score (F1), and mean intersection over union (mIOU) are used for evaluation.

Training Details – All models were trained for 200 epochs using cross-entropy loss and the SGD optimizer (initial learning rate: 0.001) on an NVIDIA RTX 4060 Ti GPU. A ReduceLROnPlateau scheduler was used with a minimum learning rate of 10^{-6} . We follow the protocol of SOTA adversarial training strategy [46] to set up our experiments on our diverse datasets.

Adversarial Evaluation – Robust-MAIL is tested under white-box attacks PGD [35], BIM [30], and MIM [16], using $\epsilon = \frac{4}{255}$, step size $\alpha = \frac{10}{255}$, and 10–100 iterations. For black-box robustness, we adopt AutoAttack (AA) [9] and Square [2] with ResNet101 as the surrogate. All experiments are implemented in TensorFlow.

4.1 Performance Comparisons

In summary, our MAIL network achieved exceptional performance across 20 diverse medical imaging datasets, with classification (D1–D16) and segmentation (D17–D20) results between 70.69% and 100%. As shown in Tables 1–2, MAIL surpassed SOTA single-modal learning and MFL methods with 0.2%–13.9% improvements across

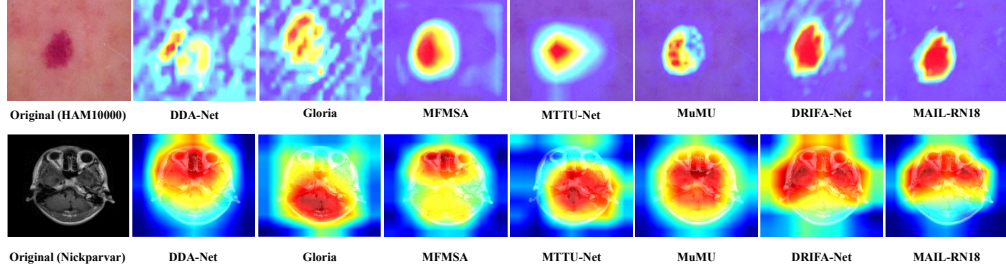


Figure 7: Visual representation of the important regions highlighted by our proposed MAIL networks i.e., MAIL-RN18 and MAIL-RN50 and ten SOTA methods using the GRAD-CAM technique on two benchmark datasets D5 and D1.

all metrics. We conducted a qualitative analysis on the D1 and D5 datasets further validate its effectiveness (ref. Figs. 7).

As discussed earlier, MAIL outperforms prior methods due to their limited applicability across diverse medical imaging modalities. Although DRIFA-Net performs well, it is resource-intensive attention modules incur high computational costs, limiting its applicability in resource-constrained environments. Our MAIL method **addresses challenge 2** by parallelizing the fusion of the MFIFA and EMSCA modules, ensuring balanced contributions from both, thereby effectively capturing complementary shared representations (**addressing challenge 3**) [12]. By leveraging the ERLA and EMCAM, MAIL achieves optimal performance while minimizing computational costs. This design leads to performance gains of 0.2%–1.9% while significantly reducing computational cost – achieving 54.9%–81.3% fewer parameters and FLOPs compared to top competitors (**tackling challenge 1**) [44].

4.2 Impact of Robust-MAIL Network

As shown in Fig. 1, the baselines along with MAIL framework exhibits significant vulnerability to adversarial perturbations, underscoring the need for robust architectures to ensure reliability in AI-driven healthcare applications. To address this, we propose Robust-MAIL, which consistently outperforms SOTA defenses across six diverse datasets, achieving up to 9.34% performance gains over leading competitors (Table 3), **addressing the limitations outlined in challenge 4**. Unlike existing methods that rely on a single defense approach, such as attention noise injection or RPF, our method uniquely integrates multiple defenses, including MAN and RPF, to achieve comprehensive robustness.

Evaluation with Stronger Attacks: We further evaluated Robust-MAIL on D5 and D3 datasets under stronger PGD attacks with increased iterations from 10 to 100 and larger perturbations $\epsilon \in [0.01, \dots, 0.1]$ (Fig. 6). Despite this situation, Robust-MAIL outperformed the best SOTA defenses, achieving up to 6.72% higher performance under PGD-100. These results underscore Robust-MAIL’s superiority in protecting MAIL against stronger adversarial attacks.

4.3 Ablation Study

Ablation of each component of MAIL. We evaluated the contribution of each component in MAIL on the D5 and D6 datasets, focusing on the ERLA block and the MFIFA and EMSCA modules of EMCAM. As shown in Table 4, the MAIL network, incorporating all modules, outperformed variants missing any module, with gains

ranging from 0.5% to 7.4%, highlighting the effectiveness of the integrated design.

Ablation of sub-components. We further analyzed individual contributions of MSGDC and CA in EMILA; the composition operation (CO) (ref. section 3.1.2) and diverse frequency (DF) (ref. section 3.1.2) – in the MFIFA, and the role of MSGDC and cross-modal interaction (CMI) in the EMSCA module. As shown in Table 5, MAIL, integrating all components, achieved performance gains of up to 6.2% over partial configurations.

Ablation of cascaded vs. parallel fusion attention. Table 6 further shows that MAIL, with parallel fusion attention, outperforms cascaded attention by up to 0.4%, highlighting the benefit of parallel information integration.

Discussion. One can infer that the limited performance of ablated variants (Tables 4–5) can be attributed to their inability to capture effective complementary shared representations while maintaining low computational costs – crucial for **addressing challenge 1**. Also, cascaded attention architectures suffer from progressive information loss during inter-module transitions, primarily due to the absence of parallel fusion mechanisms among attention modules. This limitation restricts holistic information preservation, impedes effective representation learning, and ultimately degrades performance (ref. Table 6) [32, 50]. On the other hand, MAIL’s design preserves holistic information across modules to mitigate information loss, thus leading to superior performance in multi-disease classification with minimal computational cost (Table 6). To demonstrate adversarial robustness, we evaluated RPF in the ERLA block (denoted as RPF@E) and at EMCAM, alongside MAN in Robust-MAIL on D5 and D3. As reported in Table 5, Robust-MAIL outperforms all variants lacking any defense components, achieving improvements of up to 65%. These results highlight the crucial role of each defense module in enhancing robustness.

5 Conclusion

We propose MAIL, which uses efficient multimodal cross attention module to unlock the full potential of shared representation learning across diverse modalities for classification and segmentation tasks in medical imaging. To ensure adversarial robustness, we introduce Robust-MAIL. Extensive evaluations demonstrate that our approach effectively utilizes the synergy across modalities and tasks, learning effective shared representations for multi-disease classification while ensuring adversarial robustness. Future work will explore advanced multi-omics analysis and stronger adversarial defenses.

References

- [1] Hamdalla Alyasriy and A Muayed. 2020. The IQ-OTHNCCD lung cancer dataset. *Mendeley Data* 1, 1 (2020), 1–13.
- [2] Maksym Andriushchenko, Francesco Croce, Nicolas Flammarion, and Matthias Hein. 2020. Square attack: a query-efficient black-box adversarial attack via random search. In *European conference on computer vision*. Springer, 484–501.
- [3] Vijay Badrinarayanan, Alex Kendall, and Roberto Cipolla. 2017. Segnet: A deep convolutional encoder-decoder architecture for image segmentation. *IEEE transactions on pattern analysis and machine intelligence* 39, 12 (2017), 2481–2495.
- [4] Patrick Bilic, Patrick Christ, Hongwei Bran Li, Eugene Vorontsov, Avi Ben-Cohen, Georgios Kaassis, Adi Szeskin, Colin Jacobs, Gabriel Efrain Humpire Mamani, Gabriel Chartrand, et al. 2023. The liver tumor segmentation benchmark (lits). *Medical Image Analysis* 84 (2023), 102680.
- [5] Hu Cao, Yueyue Wang, Joy Chen, Dongsheng Jiang, Xiaopeng Zhang, Qi Tian, and Manning Wang. 2022. Swin-unet: Unet-like pure transformer for medical image segmentation. In *European conference on computer vision*. Springer, 205–218.
- [6] Jieneng Chen, Yongji Lu, Qihang Yu, Xiangde Luo, Ehsan Adeli, Yan Wang, Le Lu, Alan L Yuille, and Yuyin Zhou. 2021. Transunet: Transformers make strong encoders for medical image segmentation. *arXiv preprint arXiv:2102.04306* (2021).
- [7] J. Cheng, J. Liu, H. Kuang, and J. Wang. 2022. A Fully Automated Multimodal MRI-Based Multi-Task Learning for Glioma Segmentation and IDH Genotyping. *IEEE Transactions on Medical Imaging* 41, 6 (June 2022), 1520–1532. doi:10.1109/tmi.2022.3142321
- [8] Noel Codella, Veronica Rotemberg, Philipp Tschandl, M Emre Celebi, Stephen Dusza, David Gutman, Brian Helba, Aadi Kalloo, Konstantinos Liopyris, Michael Marchetti, et al. 2019. Skin lesion analysis toward melanoma detection 2018: A challenge hosted by the international skin imaging collaboration (isic). *arXiv preprint arXiv:1902.03368* (2019).
- [9] Francesco Croce and Matthias Hein. 2020. Reliable evaluation of adversarial robustness with an ensemble of diverse parameter-free attacks. In *International conference on machine learning*. PMLR, 2206–2216.
- [10] Y. Cui, Y. Tao, W. Ren, and A. Knoll. 2023. Dual-domain attention for image deblurring. In *Proceedings of the AAAI Conference on Artificial Intelligence*, Vol. 37. 479–487.
- [11] Joy Dhar, Kapil Rana, and Puneet Goyal. 2024. Uncertainty-RIFA-Net: Uncertainty Aware Robust Information Fusion Attention Network for Brain Tumors Classification in MRI Images. In *International Conference on Pattern Recognition*. Springer, 311–327.
- [12] Joy Dhar, Nayyar Zaidi, Maryam Haghighe, Puneet Goyal, Sudipta Roy, Azadeh Alavi, and Vikas Kumar. 2024. Multimodal Fusion Learning with Dual Attention for Medical Imaging. *arXiv preprint arXiv:2412.01248* (2024).
- [13] Bo Dong, Wenhui Wang, Deng-Ping Fan, Jinpeng Li, Huazhu Fu, and Ling Shao. 2021. Polyp-pvt: Polyp segmentation with pyramid vision transformers. *arXiv preprint arXiv:2108.06932* (2021).
- [14] J. Dong, J. Chen, X. Xie, J. Lai, and H. Chen. 2023. Adversarial Attack and Defense for Medical Image Analysis: Methods and Applications. *arXiv preprint arXiv:2303.14133* (2023).
- [15] Minjing Dong and Chang Xu. 2023. Adversarial robustness via random projection filters. In *Proceedings of the IEEE/CVF Conference on Computer Vision and Pattern Recognition*. 4077–4086.
- [16] Yinpeng Dong, Fangzhou Liao, Tianyu Pang, Hang Su, Jun Zhu, Xiaolin Hu, and Jianguo Li. 2018. Boosting adversarial attacks with momentum. In *Proceedings of the IEEE conference on computer vision and pattern recognition*. 9185–9193.
- [17] Rebecca C Fitzgerald, Antonis C Antoniou, Ljiljana Fruk, and Nitzan Rosenfeld. 2022. The future of early cancer detection. *Nature medicine* 28, 4 (2022), 666–677.
- [18] Tingting Han, Sebastian Nebelung, Fabio Pedersoli, Marvin Zimmermann, Mathis Schulze-Hagen, Marcus Ho, and Daniel Truhn. 2021. Advancing diagnostic performance and clinical usability of neural networks via adversarial training and dual batch normalization. *Nature communications* 12, 1 (2021), 4315.
- [19] Ali Hassani, Steven Walton, Jiachen Li, Shen Li, and Humphrey Shi. 2023. Neighborhood attention transformer. In *Proceedings of the IEEE/CVF Conference on Computer Vision and Pattern Recognition*. 6185–6194.
- [20] Kaiming He, Xiangyu Zhang, Shaoqing Ren, and Jian Sun. 2016. Deep residual learning for image recognition. In *Proceedings of the IEEE conference on computer vision and pattern recognition*. 770–778.
- [21] X. He, Y. Wang, S. Zhao, and X. Chen. 2023. Co-attention fusion network for multimodal skin cancer diagnosis. *Pattern Recognition* 133 (2023), 108990.
- [22] Zhezhi He, Adnan Siraj Rakin, and Deng Fan. 2019. Parametric noise injection: Trainable randomness to improve deep neural network robustness against adversarial attack. In *Proceedings of the IEEE/CVF Conference on Computer Vision and Pattern Recognition*. 588–597.
- [23] S. C. Huang, L. Shen, M. P. Lungren, and S. Yeung. 2021. Gloria: A Multimodal Global-Local Representation Learning Framework for Label-Efficient Medical Image Recognition. In *Proceedings of the IEEE/CVF International Conference on Computer Vision*. 3942–3951.
- [24] Md Mofijul Islam and Tariq Iqbal. 2020. Hamlet: A hierarchical multimodal attention-based human activity recognition algorithm. In *2020 IEEE/RSJ International Conference on Intelligent Robots and Systems (IROS)*. IEEE, 10285–10292.
- [25] M. M. Islam and T. Iqbal. 2022. Mumu: Cooperative Multitask Learning-based Guided Multimodal Fusion. In *Proceedings of the AAAI Conference on Artificial Intelligence*, Vol. 36. 1043–1051.
- [26] Ahmadreza Jedd, Mohammad Javad Shafiee, Michelle Karg, Christian Schäferberger, and Alexander Wong. 2020. Learn2perturb: an end-to-end feature perturbation learning to improve adversarial robustness. In *Proceedings of the IEEE/CVF Conference on Computer Vision and Pattern Recognition*. 1241–1250.
- [27] Debesh Jha, Pia H Smedsrød, Michael A Riegler, Pål Halvorsen, Thomas De Lange, Dag Johansen, and Håvard D Johansen. 2020. Kvasir-seg: A segmented polyp dataset. In *MultiMedia modeling: 26th international conference, MMM 2020, Daegu, South Korea, January 5–8, 2020, proceedings, part II* 26. Springer, 451–462.
- [28] Hamid Reza Vaezi Jozé, Amirreza Shaban, Michael Luzzolino, and Kazuhito Koishida. 2020. MMTM: Multimodal transfer module for CNN fusion. In *Proceedings of the IEEE/CVF conference on computer vision and pattern recognition*. 13289–13299.
- [29] Jakob Nikolas Kather, Cleo-Aron Weis, Francesco Bianconi, Susanne M Melchers, Lothar R Schad, Timo Gaiser, Alexander Marx, and Frank Gerrit Zöllner. 2016. Multi-class texture analysis in colorectal cancer histology. *Scientific reports* 6, 1 (2016), 1–11.
- [30] Alexey Kurakin, Ian J Goodfellow, and Samy Bengio. 2018. Adversarial examples in the physical world. In *Artificial Intelligence Safety and Security*. Chapman and Hall/CRC, 99–112.
- [31] Chang Liu, Henghui Ding, Yulun Zhang, and Xudong Jiang. 2023. Multi-modal mutual attention and iterative interaction for referring image segmentation. *IEEE Transactions on Image Processing* 32 (2023), 3054–3065.
- [32] Cheng Lv, Enxu Zhang, Guowei Qi, Fei Li, and Jiaofei Huo. 2024. A lightweight parallel attention residual network for tile defect recognition. *Scientific Reports* 14, 1 (2024), 21872.
- [33] Mengmeng Ma, Jian Ren, Long Zhao, Sergey Tulyakov, Cathy Wu, and Xi Peng. 2021. Smil: Multimodal learning with severely missing modality. In *Proceedings of the AAAI Conference on Artificial Intelligence*, Vol. 35. 2302–2310.
- [34] Yanxiang Ma, Minjing Dong, and Chang Xu. 2024. Adversarial robustness through random weight sampling. *Advances in Neural Information Processing Systems* 36 (2024).
- [35] Aleksander Madry, Aleksandar Makelov, Ludwig Schmidt, Dimitris Tsipras, and Adrian Vladu. 2017. Towards deep learning models resistant to adversarial attacks. *arXiv preprint arXiv:1706.06083* (2017).
- [36] Bjoern H Menze, Andras Jakab, Stefan Bauer, Jayashree Kalpathy-Cramer, Keyvan Farahani, Justin Kirby, Yuliya Burren, Nicole Porz, Johannes Slotboom, Roland Wiest, et al. 2014. The multimodal brain tumor image segmentation benchmark (BRATS). *IEEE transactions on medical imaging* 34, 10 (2014), 1993–2024.
- [37] S Mourya, S Kant, P Kumar, A Gupta, and R Gupta. 2019. ALL Challenge Dataset of ISBI. 2019. *The Cancer Imaging Archive* (2019).
- [38] Ju-Hyeon Nam, Nur Suriza Syazwany, Su Jung Kim, and Sang-Chul Lee. 2024. Modality-agnostic Domain Generalizable Medical Image Segmentation by Multi-Frequency in Multi-Scale Attention. In *Proceedings of the IEEE/CVF Conference on Computer Vision and Pattern Recognition*. 11480–11491.
- [39] Msoud Nickparvar. 2021. Brain tumor MRI dataset. Data set. <https://doi.org/10.34740/KAGGLE/DSV/2645886> Accessed on 3rd March.
- [40] Ozan Oktay, Jo Schlemper, Loic Le Folgoc, Matthew Lee, Matthias Heinrich, Kazunari Misawa, Kensaku Mori, Steven McDonagh, Nils Y Hammerla, Bernhard Kainz, et al. 2018. Attention u-net: Learning where to look for the pancreas. *arXiv preprint arXiv:1804.03999* (2018).
- [41] Xiaokang Peng, Yake Wei, Andong Deng, Dong Wang, and Di Hu. 2022. Balanced multimodal learning via on-the-fly gradient modulation. In *Proceedings of the IEEE/CVF conference on computer vision and pattern recognition*. 8238–8247.
- [42] Maria E Plissiti, Panagiotis Dimitrakopoulos, Giorgos Sfikas, Christophoros Nikou, Orestis Krikoni, and Avraam Charchanti. 2018. Sipakmed: A new dataset for feature and image based classification of normal and pathological cervical cells in pap smear images. In *2018 25th IEEE International Conference on Image Processing (ICIP)*. IEEE, 3144–3148.
- [43] Konstantin Pogorelov, Kristin Ranheim Randel, Carsten Griwodz, Sigrun Losada Eskeland, Thomas de Lange, Dag Johansen, Conetto Spampinato, Duc-Tien Dang-Nguyen, Mathias Lux, Peter Thelin Schmidt, et al. 2017. Kvasir: A multi-class image dataset for computer aided gastrointestinal disease detection. In *Proceedings of the 8th ACM on Multimedia Systems Conference*. 164–169.
- [44] Md Mostafijur Rahman, Mustafa Munir, and Radu Marculescu. 2024. Emcad: Efficient multi-scale convolutional attention decoding for medical image segmentation. In *Proceedings of the IEEE/CVF Conference on Computer Vision and Pattern Recognition*. 11769–11779.
- [45] Tawsifur Rahman, Amith Khandakar, Muhammad Abdul Kadir, Khandaker Rejaul Islam, Khandakar F Islam, Rashid Mazhar, Tahir Hamid, Mohammad Tariqul Islam, Saad Kashem, Zaid Bin Mahbub, et al. 2020. Reliable tuberculosis detection using chest X-ray with deep learning, segmentation and visualization. *Ieee Access* 8 (2020), 191586–191601.

[46] Leslie Rice, Eric Wong, and J. Zico Kolter. 2020. Overfitting in adversarially robust deep learning. In *Proceedings of the International Conference on Machine Learning*. PMLR, 8093–8104.

[47] Olaf Ronneberger, Philipp Fischer, and Thomas Brox. 2015. U-net: Convolutional networks for biomedical image segmentation. In *Medical image computing and computer-assisted intervention—MICCAI 2015: 18th international conference, Munich, Germany, October 5–9, 2015, proceedings, part III* 18. Springer, 234–241.

[48] Mark Sandler, Andrew Howard, Menglong Zhu, Andrey Zhmoginov, and Liang-Chieh Chen. 2018. Mobilenetv2: Inverted residuals and linear bottlenecks. In *Proceedings of the IEEE conference on computer vision and pattern recognition*. 4510–4520.

[49] R Sawyer-Lee, F Gimenez, A Hoogi, and D Rubin. 2016. Curated Breast Imaging Subset of Digital Database for Screening Mammography (CBIS-DDSM)[skup podataka]. *The cancer imaging archive* (2016).

[50] Yunhang Shen, Liujuan Cao, Zhiwei Chen, Baochang Zhang, Chi Su, Yongjian Wu, Feiyue Huang, and Rongrong Ji. 2021. Parallel detection-and-segmentation learning for weakly supervised instance segmentation. In *Proceedings of the IEEE/CVF International Conference on Computer Vision*. 8198–8208.

[51] Shenggan. 2018. BCCD Dataset. https://github.com/Shenggan/BCCD_Dataset Accessed: 2024-08-06.

[52] Lin Song, Yukang Chen, Shuai Yang, Xiaohan Ding, Yixiao Ge, Ying-Cong Chen, and Ying Shan. 2024. Low-Rank Approximation for Sparse Attention in Multi-Modal LLMs. In *Proceedings of the IEEE/CVF Conference on Computer Vision and Pattern Recognition*. 13763–13773.

[53] Lei Sun, Christos Sakaridis, Jingyun Liang, Qi Jiang, Kailun Yang, Peng Sun, Yaozu Ye, Kaiwei Wang, and Luc Van Gool. 2022. Event-based fusion for motion deblurring with cross-modal attention. In *European conference on computer vision*. Springer, 412–428.

[54] Philipp Tschandl, Cliff Rosendahl, and Harald Kittler. 2018. The HAM10000 dataset, a large collection of multi-source dermatoscopic images of common pigmented skin lesions. *Scientific data* 5, 1 (2018), 1–9.

[55] A Vaswani. 2017. Attention is all you need. *Advances in Neural Information Processing Systems* (2017).

[56] Yikai Wang, Fuchun Sun, Ming Lu, and Anbang Yao. 2020. Learning deep multi-modal feature representation with asymmetric multi-layer fusion. In *Proceedings of the 28th ACM International Conference on Multimedia*. 3902–3910.

[57] Kun Xiang, Xing Zhang, Jinwen She, Jinpeng Liu, Haohan Wang, Shiqi Deng, and Shancheng Jiang. 2023. Toward robust diagnosis: A contour attention preserving adversarial defense for covid-19 detection. In *Proceedings of the AAAI Conference on Artificial Intelligence*, Vol. 37. 2928–2937.

[58] Jiancheng Yang, Rui Shi, Donglai Wei, Zequan Liu, Lin Zhao, Bilian Ke, Hanspeter Pfister, and Bingbing Ni. 2023. Medmnist v2-a large-scale lightweight benchmark for 2d and 3d biomedical image classification. *Scientific Data* 10, 1 (2023), 41.

[59] Yundong Zhang, Huiye Liu, and Qiang Hu. 2021. Transfuse: Fusing transformers and cnns for medical image segmentation. In *Medical image computing and computer assisted intervention—MICCAI 2021: 24th international conference, Strasbourg, France, September 27–October 1, 2021, proceedings, Part I* 24. Springer, 14–24.

[60] Ce Zheng, Xianpeng Liu, Guo-Jun Qi, and Chen Chen. 2023. Potter: Pooling attention transformer for efficient human mesh recovery. In *Proceedings of the IEEE/CVF Conference on Computer Vision and Pattern Recognition*. 1611–1620.

[61] Wuji Zhou, Shaohua Dong, Meixin Fang, and Lu Yu. 2023. CACFNet: Cross-modal attention cascaded fusion network for RGB-T urban scene parsing. *IEEE Transactions on Intelligent Vehicles* (2023).

[62] Zongwei Zhou, Md Mahfuzur Rahman Siddiquee, Nima Tajbakhsh, and Jianming Liang. 2018. Unet++: A nested u-net architecture for medical image segmentation. In *Deep learning in medical image analysis and multimodal learning for clinical decision support: 4th international workshop, DLMIA 2018, and 8th international workshop, ML-CDS 2018, held in conjunction with MICCAI 2018, Granada, Spain, September 20, 2018, proceedings* 4. Springer, 3–11.

Appendix A RPF: Random Projection Filter

To improve the adversarial robustness of the proposed MAIL network, we introduce Robust-MAIL by incorporating Random Projection Filters (RPF) into the MSGDC blocks of the EMILA and EMSCA modules, following [15]. Concretely, we replace a subset of the standard learnable convolution kernels with fixed random projection filters. This randomization reduces an attacker’s ability—especially in white-box settings—to craft perturbations that reliably exploit learned filter structures. Nevertheless, aggressively increasing the proportion of random projections can inject substantial noise and hinder optimization.

To balance this trade-off, Robust-MAIL adopts a mixed design: only a fraction of convolution kernels in the MSGDC blocks are replaced by RPFs. In contrast, RPAN replaces all convolution kernels in each convolutional layer with random projection filters to further strengthen adversarial robustness.

Formally, consider an input feature map $x_i \in \mathbb{R}^{n \times n \times d} = X$, where n and d denote the spatial resolution and the channel dimension, respectively. Let $R \in \mathbb{R}^{r \times r \times d}$ be a random projection filter of a kernel size r . The output feature map z is computed as:

$$z(p, q) = R * [x]_{p, q}^r = \sum_{i=0}^{r-1} \sum_{j=0}^{r-1} \sum_{k=0}^{d-1} R(i, j, k) \cdot x(p+i, q+j, k) \text{ s.t. } \forall_i \quad (19)$$

where $[x]_{p, q}^r$ denotes the $r \times r$ subregion of x_i , spanning rows p to $p+r-1$ and columns q to $q+r-1$, used for the convolution operation.

Appendix B Extending Details of RPAN

To ensure the adversarial robustness of the MAIL network and enable reliable predictions across diverse medical imaging modalities, we propose the Robust-MAIL network. This framework integrates the Random Projection with Attention Noise (RPAN) approach, which redesigns the EMCAM and ERLA blocks by incorporating Random Projection Filters (RPFs) and Modulated Attention Noise (MAN), thereby establishing a robust defense mechanism. The RPAN consists of two core steps:

Redesigning the ERLA Block. We redesign the group point-wise convolution (GPC) and depthwise convolution (DWC) layers in the MSGDC module of the ERLA block by replacing their convolution filters with random projection filters. Inspired by [15], we substitute these filters with RPFs denoted as $\mathcal{R}_1, \dots, \mathcal{R}_{N_{R_E}}$ across the various scales of the MSGDC. This modification reformulates MSGDC within the ERLA block of the MAIL network, thereby yielding Robust-MAIL and transforming Eq. (2) into:

$$\text{MSGDC}(x) = \theta \left(\bigvee_{k \in \{3,5\}} \text{DWC}_k(\mathcal{R}_{1:N_{R_E}} * (x_i)), \text{GPC}(\mathcal{R}_{1:N_{R_E}} * (x_i)) \right) \quad (20)$$

We further reformulate the channel attention maps A_c into attention noise maps by injecting modulated attention noise into the Channel Attention (CA) mechanism (refer to Section 3.3). This is achieved by redesigning Eq. 4 into Eq. 12. The resulting attention noise is then used to learn enhanced modality-specific noisy representations x' , thereby improving adversarial robustness.

These modulated attention noise maps are generated by leveraging learnable feature layer noise through an iterative fusion strategy. This strategy integrates channel-wise noise tensor weights with trainable random noise (ref. Eq. 22). It enables the effective and adversarially robust learning of rich noisy contexts tailored to each modality-specific pattern.

$$\text{CA}(x') = x' \times \sigma \left(f_{[1:2]} \left(\left[\sum_{p=1}^3 G_p(x') \right] + [\mu] \right) \times \vartheta_x \times \eta'_I \right) \quad (21)$$

where μ represents $\text{GMP}(x') - \text{GAP}(x') - \text{GMN}(x')$.

In particular, to design the learnable feature layer noise— η_I —which is used to generate modulated attention noise for injection into the ERLA block, we employ an iterative refinement process on channel-wise noise tensor weights $\delta_I \in \mathbb{R}^c$, along with random noise η_I . This strategy enhances noise representation by guiding η_I to learn richer and more informative noisy patterns. During this process, δ_I is first modulated by the corresponding random noise η_I , followed by an element-wise multiplication with δ_I . The resulting intermediate noise is then further multiplied by η_I , ultimately forming the learnable feature layer noise η_I , as detailed in Eq. 22.

$$\eta_I = \eta_I \times (\delta_I + (\eta_I \times \delta_I)) \quad (22)$$

Redesigning the EMCAM Block. We redesign the group-point-wise convolution (GPC) and depthwise convolution (DWC) of the MSGDC within the EMSCA module of the EMCAM block by replacing them with RPFs. Inspired by [15], we substitute the convolution filters with random projection filters (RPFs), denoted as $\mathcal{R}_1, \dots, \mathcal{R}_{N_{R_E}}$, for each scale of the MSGDC. These RPFs reformulate the MSGDC in the EMSCA module of the EMCAM block within the MAIL network, enabling its transition into the Robust-MAIL framework. This modification effectively transforms Eq. 10 into following:

Table 7: Summary of datasets used in our study.

Dataset	Modality	Task	Classes / Labels	#Samples	Split	Remarks
Nickparvar MRI [39]	Brain MRI (T1-weighted)	Classification	Gloma (1621), Meningioma (1645), No Tumor (2000), Pituitary (1757)	7023	80%/10%/10%	Aggregated from Figshare, SAR-TAI, BrH35 datasets.
IQ-OTHNCCD [1]	Chest CT	Classification	Normal, Benign, Malignant	1098	80%/10%/10%	Lung nodule diagnosis.
Tuberculosis CXR [45]	Chest X-ray	Classification	Normal vs Tuberculosis	4200	80%/10%/10%	Binary TB screening.
BCCD [51]	Microscopy (blood smear)	Classification	Eosinophil, Lymphocyte, Monocyte, Neutrophil	9957	80%/10%/10%	Leukocyte subtype recognition.
HAM10000 [54]	Dermoscopy	Classification	7 skin lesion categories	10015	80%/10%/10%	>50% histopathology-confirmed labels.
SIPaKMeD [42]	Cytology	Classification	5 epithelial cell types	4049	80%/10%/10%	Pap smear cell classification of cervical cancer.
CRC (Colorectal Histology MNIST) [29]	Histology (H&E patches)	Classification	8 tissue classes (balanced)	5000	80%/10%/10%	Tissue micro-patches for histology typing.
C-NMC 2019 [37]	Microscopy (single-cell)	Classification	Malignant vs Healthy lymphocytes	15114	10661/1867/2586	–
Kvasir [43]	GI endoscopy	Classification	8 GI categories (e.g., ulcer, polyp)	4000	80%/10%/10%	Multi-class endoscopic findings.
CBIS-DDSM [49]	Mammography	Classification	Normal vs Cancer	10239	80%/10%/10%	Curated; biopsy-verified labels.
PathMNIST (MedMNIST) [58]	Histology patches	Classification	9 tissue classes	107180	89996/10004/7180	–
PneumoniaMNIST (MedMNIST) [58]	Chest X-ray patches	Classification	Normal vs Pneumonia	5856	4708/524/624	–
RetinaMNIST (MedMNIST) [58]	Fundus patches	Classification	5-grade diabetic retinopathy	1600	1080/120/400	–
BreastMNIST (MedMNIST) [58]	Breast ultrasound	Classification	Benign vs Malignant	780	546/78/156	–
TissueMNIST (MedMNIST) [58]	Single-cell images	Classification	8 cell types	236386	165466/23640/47280	–
OrganAMNIST (MedMNIST) [58]	Abdominal CT slices	Classification	11 organ classes	58830	34561/6491/17778	–
Kvasir-SEG [27]	GI endoscopy	Segmentation	Polyp mask (binary)	1000	80%/10%/10%	Resolutions 332×487 to 1920×1072; resized to 224×224×3.
ISIC 2018 (seg) [8]	Dermoscopy	Segmentation	Lesion mask (binary)	2594	2075/519	Resolutions 720×540 to 6708×4439; resized to 224×224×3.
BraTS 2020 [36]	Brain MRI (FLAIR/T1/T1ce/T2)	Segmentation	WT/TC/ET tumor regions	369	201/35/133	Multi-modal volumes with tumor subregion annotations; processed to 224×224×3.
LiTS [4]	Abdominal CT	Segmentation	Liver + tumor masks	201	131/70	Multi-center; manual masks; processed to 224×224×3.

$$S(x'_i) = AP(\text{MSGDC}(\mathcal{R}_{1:N_{r_\xi}} * (x'_i))) + MP(\text{MSGDC}(\mathcal{R}_{1:N_{r_\xi}} * (x'_i))) \quad (23)$$

We further reformulate the frequency-domain and spatial-domain attention maps, A_f and A_s , from the MFIFA and EMSCA modules, respectively, into frequency-domain attention noise maps A_f and spatial-domain attention noise maps A_s by injecting the aforementioned modulated attention noise into the frequency-domain attention (MFIFA) and spatial-domain attention (EMSCA) mechanisms (see Section 3.1.2.(A-B)). This is accomplished by redesigning Eqs. 9 and 12 into the following:

$$A_f = \sigma \left(\sum_{i=1}^m \left(\left(\eta'_i \times \left(\alpha_i \times \omega_{x'_i}^{l_w} \right) \right) + \left(\eta'_i \times \left(\varphi_i \times \omega_{x'_i}^h \right) \right) + \left(\eta'_i \times \left(\gamma_i \times \omega_{x'_i}^a \right) \right) \right) \right) \quad (24)$$

$$A_s = \sum_{i=1}^m \left(\eta'_i \times \left(\vartheta_i \times \left(\underbrace{S(x'_i) + S(x'_{m-i+1})}_{\text{cross-modal interaction}} + \underbrace{S(S(x'_i))}_{\text{hierarchical representation}} \right) \right) \right) \quad (25)$$

The resulting attention noise is then used to learn enhanced complementary shared noisy representations X^S , thereby improving the adversarial robustness of our MAIL network, denoted by $\mathcal{F}(\cdot)$. This strategy facilitates effective adversarially robust learning of rich shared noisy contexts.

We reformulate the multimodal attention maps A_m into multimodal attention noise maps A_m by incorporating modulated attention noise, achieved by redesigning Eq. 13 into the following:

$$A_m = \sigma \left(\eta'_i \times \left(\vartheta_f \times \text{MFIFA}(X') + \vartheta_s \times \text{EMSCA}(X') \right) \right) \quad (26)$$

This attention noise is then injected into the attention map to learn enhanced complementary shared noisy representations $X^S \in [x_1^S, \dots, x_m^S]$. **Adversarial Training with RPAN.** Given a Robust-MAIL network $\mathcal{F}(\cdot)$ with parameters β , which maps multimodal inputs $X \in x_{i \in [1:m]}$ to the logits $\mathcal{F}(X, \beta) \in \mathbb{R}^C$, where C denotes the number of output classes, the adversarial example $X^* = X + v$ is defined as:

$$\max_{X^*} \mathcal{L}_{\text{MTL}}(\mathcal{F}(X^*, \beta[A]), Y), \quad \text{s.t. } \|X^* - X\| \leq \epsilon, \quad (27)$$

where ϵ represents the maximum allowable perturbation size, and $Y = [y_1, \dots, y_t]$ is the set of ground-truth labels for t classification tasks. In the adversarial training strategy, adversarial examples are generated and fed into the Robust-MAIL network to formulate a min-max optimization problem as follows:

$$\min_{\beta[A]} \max_{X^*} \mathcal{L}_{\text{MTL}}(\mathcal{F}(X^*, \beta[A]), Y), \quad \text{s.t. } \|X^* - X\| \leq \epsilon. \quad (28)$$

With the incorporation of RPF and our modulated attention noise within RPAN, along with the adversarial training strategy described in Algorithm 2, the Robust-MAIL model demonstrates strong defense capabilities during inference, as illustrated in Fig. 1.

Appendix C Datasets Details

Our study leverages 20 diverse medical imaging datasets, we provide the details in Table 7: